remote sensing

MDPI

Article

SI-Traceability and Measurement Uncertainty of the Atmospheric Infrared Sounder Version 5 Level 1B Radiances

Thomas S. Pagano [1,*], Hartmut H. Aumann [1], Steven E. Broberg [1], Chase Cañas [1], Evan M. Manning [1], Kenneth O. Overoye [2] and Robert C. Wilson [3]

[1] Jet Propulsion Laboratory, California Institute of Technology, Pasadena, CA 91109, USA; hartmut.h.aumann@jpl.nasa.gov (H.H.A.); steven.e.broberg@jpl.nasa.gov (S.E.B.); chase.canas@jpl.nasa.gov (C.C.); evan.m.manning@jpl.nasa.gov (E.M.M.)

[2] Millenium Engineering and Integration Company, Inc., Arlington, VA 22202, USA; kroveroye@verizon.net

[3] Raytheon Company, Waltham, MA 02451, USA; robert.c.wilson@jpl.nasa.gov

* Correspondence: thomas.s.pagano@jpl.nasa.gov; Tel.: +1-818-393-3917

Received: 23 March 2020; Accepted: 21 April 2020; Published: 23 April 2020

Abstract: The Atmospheric Infrared Sounder (AIRS) on the EOS Aqua Spacecraft was launched on 4 May 2002. The AIRS is designed to measure atmospheric temperature and water vapor profiles and has demonstrated exceptional radiometric and spectral accuracy and stability in orbit. The International System of Units (SI)-traceability of the derived radiances is achieved by transferring the calibration from the Large Area Blackbody (LABB) with SI traceable temperature sensors, to the On-Board Calibrator (OBC) blackbody during preflight testing. The AIRS views the OBC blackbody and four full aperture space views every scan. A recent analysis of pre-flight and on-board data has improved our understanding of the measurement uncertainty of the Version 5 AIRS L1B radiance product. For temperatures greater than 260 K, the measurement uncertainty is better than 250 mK 1-sigma for most channels. SI-traceability and quantification of the radiometric measurement uncertainty is critical to reducing biases in reanalysis products and radiative transfer models (RTMs) that use AIRS data, as well as establishing the suitability of AIRS as a benchmark for radiances established in the early 2000s.

Keywords: infrared; hyperspectral; satellite; radiometric; calibration; sounder; polarization; accuracy; uncertainty

1. Introduction

Infrared (IR) sounders measure the upwelling spectrum of the Earth's atmosphere with high spectral resolution, as shown in Figure 1. This enables the profiling of temperature (using CO_2 absorption features) and water vapor concentrations and measurement of concentrations of trace gases. IR sounders operating today include the Atmospheric Infrared Sounder (AIRS) on the NASA Aqua satellite [1], the Cross-track Infrared Sounder (CrIS) on the NASA/NOAA Suomi NPP and NOAA JPSS satellites [2], the Infrared Atmospheric Sounding Interferometer (IASI) on the EUMETSAT MetOp satellites [3], the Hyperspectral Infrared Atmospheric Sounder (HIRAS) on the CMA FY-3 satellites [4], the Geostationary Interferometric Infrared Sounder on the CMA FY-4A satellite [5], and the advanced infrared (IR) sounder IKFS-2 on the Russian Meteor-M satellite [6]. All of these instruments are 'hyperspectral', having very high spectral resolution (>1000) enabling the resolution of CO_2 and H_2O absorption features used to make temperature and water vapor profiles. From IR sounder radiances, it is possible to retrieve trace gas constituents including O_3, CO, CH_4, and SO_2 at various altitudes from the surface to the stratosphere, depending on the constituent. The sounders also

measure surface temperature and emissivity, cloud top height, cloud liquid water and cloud fraction. The data from the IR sounders assimilated into Numerical Weather Prediction (NWP) models have demonstrated amongst the highest forecast improvement in NWP models of all data types. The data are regularly used in studies of processes affecting weather [7] and climate as well as the validation of weather and climate models [8]. The data are also used in applications including volcano alerts [9], drought prediction [10], and air quality and pollution transport [11]. The AIRS instrument has shown exceptional radiometric stability to date, making it a valuable tool for climate trending and model validation [12].

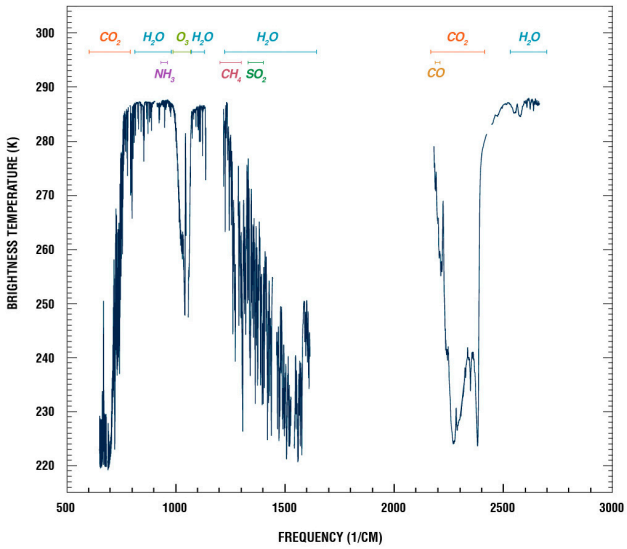

Figure 1. Typical AIRS spectrum and location of key atmospheric constituents. AIRS data are used for weather forecasting, climate process studies and validating climate models (adapted from [1]). For more information, see http://airs.jpl.nasa.gov.

The AIRS is a "facility" instrument developed by NASA and launched on the Earth Observing System (EOS) Aqua satellite on May 4, 2002, as an experimental demonstration of advanced remote sensing technology in the areas of optics, detectors, and cryocoolers, and to demonstrate the benefits of high resolution infrared spectra for weather and science. The AIRS instrument is expected to provide a ~20 continuous year record from launch in 2002, to Spring 2022, when the Aqua spacecraft is expected to exit the A-Train. As the Aqua spacecraft drifts away from the A-Train, 1:30 PM mean local crossing time, additional data valuable to weather and process studies are expected to be acquired for another 3 to 4 years. The AIRS radiances at the 1231 cm^{-1} window channel show excellent stability relative to independent SST estimates, with a drift of less than 0.2–0.3 mK/decade, from 2002 to 2019 [13]. Using retrievals of trace gases from AIRS compared to in situ measurements allows the estimation of radiance trends of several AIRS channels to as good as 0.02–0.03 mK/decade [14]. Trending over the AIRS timeframe may not require knowledge of the measurement uncertainty; however, when combining AIRS with other data sets, or establishing a benchmark, an estimate of the measurement uncertainty is essential.

AIRS data are also part of the ERA-Interim [15] and MERRA reanalyses [16]. An emerging requirement is for these models to be stable over interannual and decadal timescales. Uncertainties in the radiometric calibration of the AIRS can impact the accuracy of the reanalysis. Bias corrections, or 'tuning', of the AIRS radiances is performed prior to assimilation, but developers of the reanalyses have indicated that knowledge of the AIRS uncertainty will make it easier to differentiate between errors in their models and the AIRS measurement.

The AIRS is a reference sensor in the Global Space-Based Intercalibration of Sensors (GSICS) [17,18]. AIRS is used operationally by the Japan Meteorological Agency (JMA) for comparison to Himawari 8/9 AHI JM [19], the Korean Meteorological Administration (KMA) for comparison to COMS [20], and NOAA for comparison to CrIS [21] and GOES [22], and EUMETSAT for comparison to IASI [23]. The results show that the AIRS compares with IASI and CrIS to better than 0.2 K (1-sigma) in most cases. The long record of AIRS, combined with its stability and high accuracy, make it an important reference sensor for GSICS. Rigorous quantification of the uncertainties relative to SI standards will enable the benchmarking of the AIRS radiances, enabling trends over long periods, in the event of a break in continuity of similar IR sounder measurements.

The AIRS instrument meets the three primary elements identified in the Guidelines for Radiometric Calibration of Electro-Optical Instruments for Remote Sensing [24] as the foundation of an effective calibration: (1) traceability, (2) measurement uncertainty, and (3) verification and validation. Verification and validation of AIRS Level 1B radiances using vicarious calibration of the Earth scene can be found in the literature [13,14]. The SI-traceability, as defined in the Joint Committee for Guides in Metrology (JCGM) the Vocabulaire international de métrologie (VIM) [25] and the Guide to the expression of Uncertainty of Measurement (GUM) [26], requires an unbroken chain of calibrations, each contributing measurement uncertainty. The AIRS is traceable to the National Institute of Standards and Technology (NIST) calibrated thermistors in the LABB through pre-flight radiometric cross-calibration with the on-board calibrator (OBC) blackbody. Measurement uncertainty is defined, per the VIM and GUM, as the 'non-negative parameter characterizing the dispersion of the quantity values being attributed to a measurand', and are of two types, A and B. Type A uncertainties are obtained by statistical evaluation of the measured quantities. For AIRS, this includes statistical analysis of the pre-flight and in-orbit data used to derive the calibration coefficients. Type B uncertainties are those obtained by other means. For AIRS, this includes component measurement uncertainty combined with models, as for the LABB and Space View Source (SVS), or instrument related drift. Radiometric accuracy is not a physical quantity and is used as qualitative term to represent the closeness of the AIRS-measured radiances with the true radiance.

The AIRS radiances are computed from the observed instrument digital counts and on-board calibration data applied to the instrument radiometric calibration equation. The AIRS radiometric measurement uncertainty considers the uncertainty of all elements in the radiometric calibration equation. Each of the contributors to the radiometric uncertainty is discussed below with their uncertainty type (A or B). We then combine the uncertainties into an overall radiometric measurement uncertainty for the AIRS Version 5 Level 1B data product. The results show the measurement uncertainty to be between 100 and 600 mK (1-sigma), depending on detector module, for a scene temperature of 260 K.

2. Materials and Methods

We use a bottom-up approach to calculate the radiometric measurement uncertainty of AIRS as the combined uncertainty of all the contributors to the AIRS radiometric calibration equation, and the uncertainty of the LABB and SVS. We build on prior work [27,28] but employ more test data including observed trends in the instrument response where possible. The analysis applies to the AIRS L1B Version 5 (V5) geolocated spectral radiance product, since this product is currently available for the entire mission period. We review the origin of the V5 calibration coefficients, and take a fresh look at their uncertainty by comparing them to a new set of coefficients (candidates for Version 7 (V7)), expected to be more accurate with better uncertainty estimates [29]. The V7 coefficients and their validation use recent measurements in-orbit of the earth, space and on-board calibrators, and a more comprehensive analysis of pre-flight test data.

The on-orbit verification and validation of the radiometric calibration of AIRS is performed by comparison of AIRS measurements to scene targets such as sea surface temperature (SST) [30], trace gas concentrations [14], and by comparison to other instruments [31]. In these cases, agreement is

seen to be better than 200 mK 1-sigma. Typically, a radiative transfer model will introduce errors as high as 200 mK any time the user attempts to associate geophysical parameters to the radiances. The bottom-up approach presented here will provide an independent assessment of the uncertainty of the AIRS radiometry that can be compared to these other methods.

The analysis presented in this paper assumes spatially and spectrally uniform scenes consistent with a Planck blackbody distribution. Other errors contribute to the radiometric uncertainty including spatial co-registration errors [32], and spectral response knowledge errors [33]. Co-registration errors are scene dependent and can result in significant systematic errors, affecting 1% of the scenes and ~10% of the channels. Averaging a large number of spectra (footprints) will reduce or eliminate co-registration systematic errors, or an approach using the AIRS spatial response with MODIS imagery can greatly reduce co-registration errors on single spectra [32]. If sensitivity to channel coregistration is a concern then the flags Sceneinhomogeneous, Rdiff_swindow and Rdiff_lwindow can also be used to restrict data selection to uniform scenes. Spectral errors can be mitigated by accounting for the time dependent spectral centroids provided in the L1B product. A new release of the AIRS Level 1C product resamples the AIRS L1B to a common frequency set, fills spectral gaps, and removes obvious radiometric outliers related to co-registration errors [34]. The L1C algorithm uses principal component reconstruction (PCR) to adjust the radiances to be more representative of what would be expected without spatial errors. Using the L1C algorithm will result in lower errors for problematic channels in individual spectra, yet SI-traceability of the radiances for L1C is more complex, due to the use of the PCR, and has not yet been estimated. Since the L1C product is built on the L1B product, this analysis will serve as reference for a future uncertainty estimate of the L1C.

2.1. The AIRS Instrument

The AIRS instrument, shown in Figure 2, developed by BAE SYSTEMS, incorporates numerous advances in infrared sensing technology to achieve a high level of measurement sensitivity, precision, and accuracy [35]. This includes a temperature-controlled spectrometer (157 K) and long-wavelength cutoff HgCdTe infrared detectors cooled by an active-pulse-tube cryogenic cooler. The AIRS measures 2378 infrared spectral channels ranging from 3.7 to 15.4 μm. The 2378 spectral channels have resolutions, $\lambda/\Delta\lambda$, ranging from 1086 to 1570, in three bands: 3.75 to 4.61 μm, 6.20 to 8.22 μm, and 8.8 to 15.4 μm. The AIRS scans a single 13.5 km footprint cross-track ±49.5° or 1750 km from the orbit altitude of Aqua at 705.3 km.

Figure 2. The Atmospheric Infrared Sounder (AIRS) shown at BAE SYSTEMS prior to delivery for spacecraft integration, has provided over 17 years of global daily SI-traceable IR radiances of Earth.

The Focal Plane Assembly (FPA) contains 12 modules with 15 individual Photovoltaic (PV) HgCdTe line arrays of detectors in 2 × N element arrays where N ranges from 94 to 192 for PV HgCdTe, and 2 Photoconductive (PC) HgCdTe arrays with 1 × 144, and 1 × 130. Table 1 lists the modules.

The 2 elements for each channel in the PV HgCdTe arrays are referred to as the A and B sides of the channel. During normal operations, any given channel's signal is determined by a table, uploaded to the instrument, selecting either the A side, B side or a combination of the A and B side detectors (AB).

Table 1. Module spectral regions.

Array	Module	Wavelength (min) (μm)	Wavelength (max) (μm)
1	M1a	3.7364	3.9169
2	M1b	4.11	4.3291
3	M2a	3.9149	4.11
4	M2b	4.3271	4.6085
5	M3	6.9356	7.4769
6	M4a	6.2003	6.4934
7	M4b	6.5504	6.85
8	M4c	7.4745	7.7921
9	M4d	7.8605	8.22
10	M5	8.8073	9.4796
11	M6	9.565	10.275
12	M7	10.275	10.985
13	M8	11.0704	11.7512
14	M9	11.7431	12.685
15	M10	12.7989	13.7457
16	M11	13.7377	14.5533
17	M12	14.6672	15.4

The key to the high accuracy and SI-traceability of AIRS is the high quality OBC cavity blackbody and full aperture space view observed every scan, and a simple direct conversion of counts to radiances using a 2nd order polynomial with polarization correction. The OBC blackbody is a specular coated wedge design with an internal angle of 27.25°. The scan cavity and calibration target geometry are shown in Figure 3.

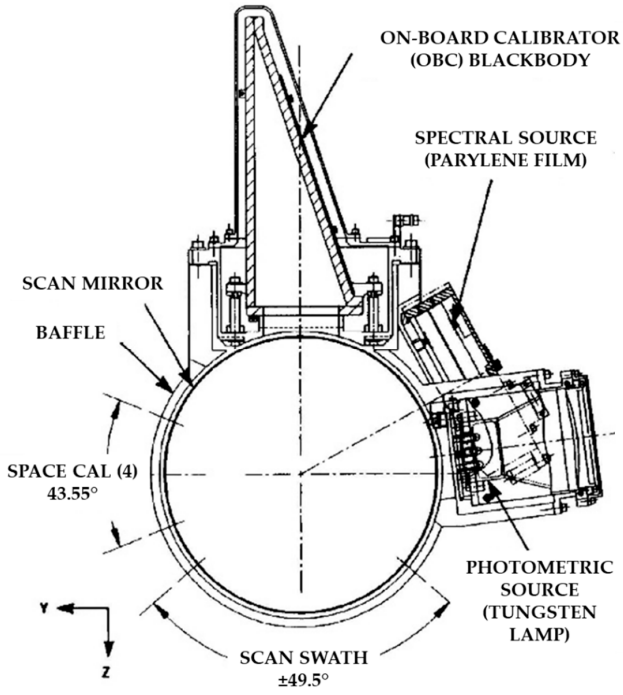

Figure 3. The AIRS scan cavity and calibration targets. Radiometric calibration is performed using views of the on-board calibrator (OBC) blackbody and space obtained on every scan.

2.2. Radiometric Calibration Equation

We can estimate the radiance of the Earth View, L_{ev}, as a second order polynomial in the difference in counts between the earth view and space view (to remove instrument background radiance), and a polarization dependent offset term due to change in orientation of the scan mirror relative to the spectrometer [29,36]. We call this the AIRS radiometric calibration equation.

$$L_{ev} = L_o(\theta) + \frac{c_0 + c_1'(dn_{ev} - dn_{sv}) + c_2(dn_{ev} - dn_{sv})^2}{[1 + p_r p_t cos2(\theta - \delta)]} \quad (1)$$

The coefficients of the radiometric calibration equation are determined using pre-flight and on-orbit tests as discussed in Section 2.6. In-flight, the gain is recalculated on-orbit for every scan using the OBC blackbody.

$$c_1' = \frac{[\varepsilon_{obc} P_{obc}(T_{obc}, \lambda) - L_o(\theta_{obc})][1 + p_r p_t cos2\delta] - c_2(dn_{obc} - dn_{sv})^2 - c_0}{(dn_{obc} - dn_{sv})} \quad (2)$$

The polarization offset, due to the coupling of the polarization of the scan mirror, can be shown to be [29]

$$L_o(\theta) = \frac{P_{sm}(T_{sm}, \lambda) p_r p_t [cos2(\theta - \delta) - cos2(\theta_{sv,i} - \delta)]}{[1 + p_r p_t cos2(\theta - \delta)]} \quad (3)$$

where we have used $\theta_{OBC} = 180°$ and $cos2(180° - \delta) = cos(2\delta)$. The OBC emissivity is obtained while viewing the LABB pre-flight using Equation (1) solving for the OBC emissivity. This constitutes the transfer of the SI-traceability from the LABB to the OBC blackbody.

$$\varepsilon_{obc} = \left\{ L_o(\theta_{obc}) + \frac{c_0 + c_1(dn_{obc} - dn_{sv}) + c_2(dn_{obc} - dn_{sv})^2}{[1 + p_r p_t cos2\delta]} \right\} / P_{obc} \quad (4)$$

where

L_{ev} = Spectral radiance in the Earth viewport (W/m^2-sr-μm)
$L_o(\theta)$ = Polarized mirror emission spectral radiance (W/m^2-sr-μm)
c_0 = Instrument offset (W/m^2-sr- μm)
c_1 = Instrument gain (W/m^2-sr- μm-counts)
c_2 = Instrument nonlinearity (W/m^2-sr- μm-counts^2)
dn_{ev} = Digital counts while viewing Earth for each footprint and scan (counts)
dn_{sv} = Median of the digital counts of the 4 space views for each scan (counts)
dn_{obc} = Digital counts while viewing the OBC Blackbody (counts)
P_{sm} = Planck spectral radiance of the scan mirror at T_{sm} (W/m^2-sr-μm)
P_{obc} = Plank spectral radiance of the OBC blackbody at temperature T_{obc} (W/m^2-sr-μm)
T_{obc} = Temperature of the OBC blackbody (K)
ε_{obc} = Effective emissivity of the blackbody (unitless)
T_{sm} = Temperature of scan mirror (K)
$p_r p_t$ =Product of scan mirror and spectrometer polarization diattenuation (unitless)
θ = Scan Angle measured from nadir in the Earth View (radians)
$\theta_{sv,i}$ = Scan Angle measured from nadir for the ith space view (i=1 to 4) (radians)
δ = Phase of spectrometer polarization (radians)

2.3. Radiometric Measurement Uncertainty Estimate Approach

The in-orbit radiometric measurement uncertainty of the AIRS relative to SI Standards is estimated as the radiometric uncertainty of the SI-traceable standards used to calibrate the instrument, the LABB

and the SVS, and the measurement uncertainty of the AIRS instrument and algorithms in being able to reproduce the calibration obtained pre-launch. The uncertainty estimates of the LABB and SVS are discussed in Section 2.5. For the AIRS instrument, as mentioned above, we fit the radiometric calibration equations to observational data pre-flight and in-orbit to arrive at a set of coefficients and uncertainties.

The AIRS V5 radiometric calibration coefficients have not changed since launch. Other changes have occurred since launch that do not affect the uncertainty including the use of averaging scans in the space view and OBC blackbody view counts within a 135-scan group (granule). We have a new set of coefficients, V7, which we believe to be more accurate, with reduced uncertainty, that is quantified below, which can then be used to estimate the uncertainty of V5.

We compute the radiometric measurement uncertainty in the V5 coefficients as the Root Sum Square (RSS) of the systematic differences between V5 and V7, and the uncertainty in the V7 coefficients. We also include the time dependence in the coefficients as uncertainty, since the V5 coefficients were static based on pre-flight values. For each coefficient, χ, we have up to three terms in the uncertainty for V5

$$\Delta\chi^{V5} = \sqrt{(\chi^{V5} - \chi^{V7})^2 + (\Delta\chi^{V7})^2 + \left(\frac{d\chi^{V7}}{dt}\Delta t\right)^2} \quad (5)$$

Combining the apparent difference between V5 and V7 with the uncertainty and drift of the reference (in this case V7) gives a full representation of the uncertainty of the term. In cases where the V7 coefficients include the drift, the drift term is not needed explicitly (see below). Since the coefficients for V7 are computed for A, B and AB PV detector sides independently, while for V5 there is only one set applied regardless of the detector side(s) in use on orbit, the V7 coefficients corresponding to the A side, B side, or AB combined in use on orbit in October 2019 is used when comparing to V5.

2.4. Radiometric Uncertainty Contributors

Using the radiometric calibration equations, we identify 14 primary contributors to the radiometric uncertainty of the AIRS instrument and the pre-flight ground calibration targets. The entries in Table 2 represent the average over all modules of the median over all channels within the module. Uncertainty type (A or B) is identified in the description. Uncertainties are expressed in their native units and include systematic differences (V5-V7), uncertainty of V7 coefficients, and drift where appropriate. Uncertainties for the V7 coefficients are computed for every channel as the standard deviation of the coefficients derived from each test for a given AB PV detector side. Errors will be slightly higher in V5 for channels which have changed the PV detector side from A to B during the mission, since V5 carried only one coefficient for both sides. These errors will show up when we take the difference with V7, which accounted for the individual PV detector side. Dead or very noisy pixels (about 100 of the 2378) are given coefficients based on their neighbors and should not be used. The AB PV detector configuration and noise properties for all channels is identified in the instrument channel properties files at the Goddard Earth Sciences Data and Information Services Center (GES DISC) for the given epoch.

The temperature and emissivity of the LABB and SVS are assumed to be constant for all modules (wavelength). Instrument scan mirror temperature, OBC temperature and angle uncertainty are also fixed for all modules. The calibration coefficients' uncertainties, $\Delta p_r p_t$, $\Delta\delta$, Δa_o, Δa_2, and $\Delta\varepsilon_{OBC}$, are calculated for each channel independently, as well as the correlated noise, NEN_{corr}, and the drift, Δdn. The highest errors are due to the uncertainties in the polarization, offset, and nonlinearity coefficients. We discuss the individual contributors to uncertainty in more detail below. The total uncertainty identified in Table 2 is the RSS of the contributors in the table and is an overall figure of merit for the instrument. Section 3 provides more detail on the behavior of each module.

Table 2. Contributors to the AIRS radiometric measurement uncertainty (Uncty.) expressed in their native units (N.U.) and as a temperature uncertainty at 260 K. All values are 1-sigma, and represent the average over all modules of the median over all channels within the module. Error type (A or B) is given for each contributor.

	Description	Nominal (N.U.)	Uncty. (N.U.)	Uncty. (mK)
	Uncertainty of Ground Based Reference Sources			
1	LABB Temperature (K) • Based surface temperature uncertainty and model (B)	260	0.030	30.2
2	LABB Emissivity (-) • Based on surface reflectance measurements and model (B)	0.99994	0.00006	2.5
3	SVS Temperature (K) • Based on surface temperature uncty. and model cavity (B)	85	1.0	0.6
4	SVS Emissivity (-) • Based on surface reflectance measurements and model (B)	0.9998	0.0002	0.0
	Uncertainty of the AIRS Instrument			
5	Scan Mirror Temperature (K) • Driven by time lag in sensor readout (B)	260	0.67	0.9
6	Scan Angle (r) • Driven by pixel cross-track scanning (B)	0	0.0096	0.1
7	Polarization Product (-) • Includes V7-V5 (A), V7 StdDev over tests (A), and drift (B)	9.04×10^{-4}	0.00180	71.6
8	Polarization Phase. (r) • V5 had $\delta = 0$, Includes V7-V5 (A), V7 StdDev over tests (A), and drift (B)	0.80	0.91	71.1
9	Offset (W/m^2-sr-um) • V5 had $a_0 = 0$. May be residual test-related error	2.30×10^{-4}	0.0040	54.9
10	Nonlinearity (W/m^2-sr-um-dn^2) • Includes V7-V5 (A) and V7 StdDev over tests (A)	-4.06×10^{-9}	5.99×10^{-9}	56.5
11	OBC Emissivity (-) • Includes V7-V5 (A), V7 StdDev over tests (A), and drift (B)	0.9980	0.0027	82.5
12	OBC Temperature (K) • This term is for in-orbit variability (A)	308	0.0038	0.0
13	Correlated Noise (W/m^2-sr-um) • Based on pre-flight tests (A). Nominal here is the NEN.	0.015	0.0030	51.2
14	Drift per Scan • Based on pre-flight tests (A). Nominal here is viewing OBC.	3000	0.15	3.4
	RSS Total of Above Terms			163.5

2.5. Pre-Flight Radiometric Calibration Targets

The radiometric uncertainty of the LABB and the SVS is determined for AIRS by the uncertainty of the temperature sensors, and an estimate of the uncertainty in the temperature and emissivity of the target. We assume the target behaves as a Planck radiator with a computed emissivity and temperature due to the exceptionally high emissivity. We consider the reflected component (1-emissivity) to be a full radiance error. The uncertainty of the temperature of the targets is determined by measurement at the manufacturer's facility with results provided below. The uncertainty in the emissivity is determined by analysis using component measurements of surface properties of the paint, and the wedge design of the cavity. We expect additional uncertainties in the true output of the LABB and SVS and rely on multiple test and viewing geometries (nadir and 40 degrees) during testing with AIRS to capture these errors in the uncertainty estimates for the instrument.

2.5.1. LABB Temperature Uncertainty

The ground calibration LABB is a specular wedge cavity design which provides superior performance over traditional diffuse cavity blackbodies when used with instruments with a narrow field of view (1.1 degrees × 0.6 degree for AIRS). Figure 4a shows a cross-section of the cavity, and Figure 4b shows the completed assembly. Its specifications, design and tested performance were provided in [37]. The thermometers used in the LABB provide the traceability of its calibration to

the SI standards provided by NIST. These sensors are model 162D Platinum Resistance Temperature (PRT) sensors manufactured by Rosemount Aerospace (now Emerson), and were provided with NIST traceable temperature calibrations accurate to ±1 mK, or better. The cavity walls are made of 6.25 mm thick aluminum for high thermal conductivity and low temperature differentials. The sloping wall, which is directly viewed by the instrument being calibrated, is 12.5 mm thick for even better uniformity of temperature over this most critical surface. The temperatures on the sloping wall are measured in two places by the 162D sensors. Temperatures of the other walls are measured by several Rosemount model 146MC PRTs, which were calibrated against the 162D devices. The cavity wall temperature is servo controlled in 4 zones, as shown in the figure. The control sensors are the two 162D sensors (Zones 4 and 3), a 146MC sensor in the top horizontal wall (Zone 2) and a 146MC sensor in the faceplate of the cavity (Zone 1). Two other 146MC sensors monitor the bottom horizontal wall temperature (two places) and two more monitor the cavity side wall temperatures. Another sensor monitors and controls the temperature of the front aperture plate. This grooved plate, painted with diffuse black paint (Aeroglaze Z306) and held within a small fraction of a degree of the cavity temperature, surrounds the aperture of the LABB. This feature ensures that any small out-of-field response of the instrument senses very nearly the same radiance as its in-field response.

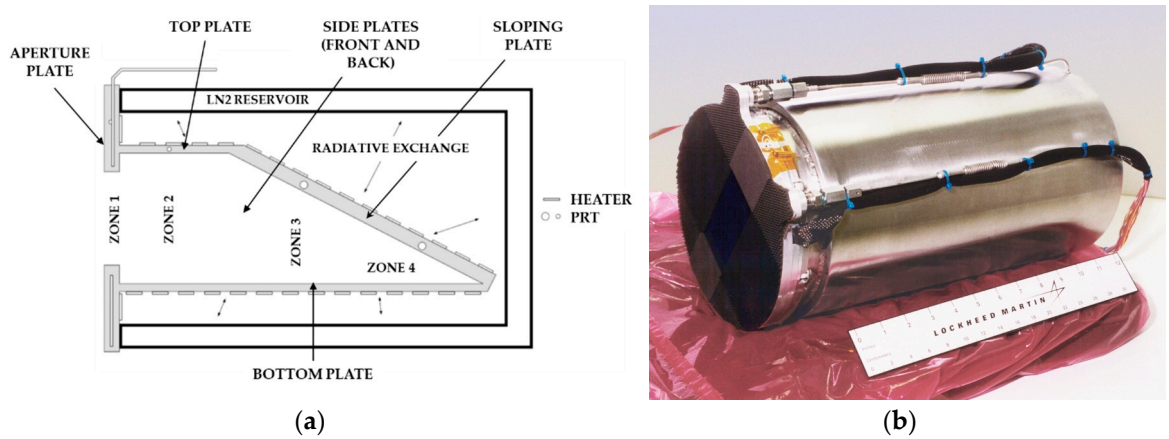

Figure 4. Large area blackbody (LABB) cavity cross-section (**a**) and completed assembly (**b**).

Test data and analysis [38] show that the uncertainty of the temperatures of the interior cavity walls of the LABB vary with its operating temperature. Table 3 shows the uncertainties of the temperatures of the emitting surface of the sloping wall and the bottom horizontal wall for the lowest, middle and highest calibrating temperatures used.

Table 3. Uncertainty of the temperatures of the emitting surfaces for 3 cavity temperatures.

Cavity Temperature:	205 K	265 K	310 K
Uncertainty in Sloping Wall	0.028 K	0.047 K	0.039 K
Uncertainty in Bottom Wall	0.17 K	0.18 K	0.18 K

In the case of the wedge cavity design, even if the temperatures are not quite uniform, knowledge of the temperature differences can be used in a fairly straightforward way to correct the calculated radiance. If the directly viewed sloping surface is at a temperature T, and the horizontal surface (viewed in specular reflection from the sloping surface) is at a temperature T + ΔT, then it can be shown that the effective temperature of the cavity is

$$T_{eff} = T + \Delta T \frac{R}{1+R} \quad (6)$$

where R is the specular reflectance of both similarly treated surfaces. The uncertainty in knowledge of T_{eff} is

$$\delta T_{eff} = \delta T + \delta \Delta T \frac{R}{1+R} + \Delta T \frac{\delta R}{(1+R)^2} \quad (7)$$

where δT, δ (ΔT) and δR are the respective uncertainties in the knowledge of T, ΔT and R.

For the LABB, the reflectance R varied between 0.1 and 0.16, depending on wavelength. Taking the temperature uncertainties from Table 3 and R = 0.12 and δR = ±0.05, then the uncertainty of the temperature of the LABB as a whole, T_{eff}, for three operating temperatures are shown in Table 4. In the worst case, the three terms add linearly. However, since the uncertainties among the terms are uncorrelated, then an RSS of the terms gives a more realistic result.

Table 4. Uncertainty of the LABB temperature for 3 cavity temperatures.

Cavity Temperature:	205 K	265 K	310 K
Linear summation	0.048 K	0.067 K	0.059 K
Root Sum Square	0.034 K	0.051 K	0.044 K

We conclude that the uncertainty of the effective blackbody temperature as used to calibrate the AIRS instrument is no worse than 0.07 K (3-sigma). We round conservatively this value to 0.03 K (1-sigma).

2.5.2. LABB Emissivity Uncertainty

A very high emissivity is of importance to any blackbody used for calibration, both to make its emission spectrum approach an ideal Planck blackbody distribution and to minimize reflection into the sensor field of view of stray radiation entering the cavity, causing additional errors. The emissivity of a wedge cavity blackbody with specular surfaces is first limited by the number of internal reflections of radiation emitted from surfaces before leaving the cavity towards the entrance pupil of the sensor it is calibrating. For a narrow field of view sensor, like AIRS, the number of reflections is easily ascertained from the geometry, typically by back projecting rays from the sensor along its line of sight and seeing how many bounces are taken before the ray reemerges from the aperture of the cavity. In the case of the LABB and the AIRS field of view, that number is 6. For a nearly perfectly specular surface inside the cavity, the emissivity is given by

$$\varepsilon = 1 - R^6 - \Omega \times BRDF \quad (8)$$

where R is the internal specular reflectance, Ω is the solid angle of the LABB as viewed by AIRS, and BRDF is the bi-directional reflectance distribution function.

Specular reflectance measurements of samples of the painted interior surfaces (Aeroglaze Z302 paint) were made with 4 cm^{-1} resolution from 3.5 to 16 μm, and at an angle of incidence of 65°, corresponding to the viewing angle at the sloping surface [39]. The maximum reflectance was 16.2% which occurred at 9.5 μm. Typically, the reflectance was 15% from 10 to 15.5 μm and 13.5% or lower from 3.5 to 9 μm. Also limiting the emissivity of the wedge design is scattering from the imperfect surfaces. For the LABB, Ω = 0.1 sr for a point inside the cavity directly observed by AIRS. The BRDF was measured at 3.39 and 10.6 μm. The worst case measured backscatter BRDF was 0.0004 sr^{-1} at 10.6 μm. The specular reflectance (R^6 = 0.00002) and the scattering reflectance (Ω × BRDF = 0.00004) for the two worst case conditions (both occurring at about 10 μm) result in an estimated cavity emissivity of 0.99994. Based on the calculated emissivity, we claim the full reflected component, of 0.00006 1-sigma, as the emissivity uncertainty for the LABB.

2.5.3. SVS Temperature and Emissivity Uncertainty

The SVS is a cavity blackbody of similar wedge design as the LABB. The SVS was used in the calibration of AIRS to simulate deep space (zero) radiance. It has close to the same wedge angle as in the LABB, so that 6 reflections are again expected before an entering ray re-emerges from the cavity. Due to the larger aperture, the solid angle as viewed by AIRS, Ω, for the SVS is 0.25 sr. Its surface treatments are the same as those used in the LABB, so the specular reflectance and BRDF are the same. The SVS operating temperature is 85 K and is measured by commercially calibrated diode sensors. A fold mirror is at the entrance of the cavity of the SVS and is held at very nearly the same temperature as that of the cavity. It is a highly polished metal mirror with scatter less than 3 orders below the scatter of the cavity surfaces; hence its contribution to cavity scatter is negligible. The calculated emissivity of the SVS is 0.99988 at the worst-case wavelength. We carry an emissivity uncertainty of 0.0002 1-sigma for the SVS. The temperature uncertainty of the SVS should be comparable to that of the LABB, except the temperature is read out with a precision of 0.5 K. We use 1 K 1-sigma for the uncertainty in the SVS effective temperature based primarily on the precision of the readout.

2.6. AIRS Instrument Uncertainties

In this section, we present each of the terms contributing to the radiometric uncertainty, as shown in Table 2, related to the instrument design or calibration.

2.6.1. Scan Mirror Temperature and Angle Uncertainty

The AIRS scan mirror temperature is monitored using a non-contacting temperature sensor located at the base of the rotating shaft. The design goal was to achieve precision to 0.5 K, but verification was not performed. We do not expect a bias to occur from ground to launch as the system is in the same configuration. Absolute knowledge of the temperature is not critical for the scan mirror since the telemetered value is used pre-flight and in orbit, giving it a good relative measurement, and the uncertainties observed during pre-flight testing are contained in the uncertainties in the offset term, c_o. The primary source of uncertainty will be in the time lag of the temperature sensor to the actual mirror temperature. In orbit, we see variations in the temperature readings from the mirror due to changes in the seasonal and orbital upwelling flux from the Earth that range from 259.5 to 261.5 K. We use this value to estimate the worst-case temperature error due to a delay in the reading of 2 K, or 0.67 K 1-sigma.

The radiometric uncertainty analysis assumes a nominal scan angle of 0°. The scan mirror angle is read out with high precision using a 14-bit encoder resulting in negligible uncertainty. The dominant source of angle uncertainty is due to the use of the center of each footprint when actually the footprint is scanned cross-track 1.1 deg. We use $\frac{1}{2}$ a pixel, or 0.55 deg (1-sigma), as a conservative estimate of the uncertainty the scan angle.

2.6.2. Polarization Amplitude and Phase Uncertainty

As mentioned above, the AIRS experiences a coupling between the polarization of the scan mirror and the polarization of the spectrometer (dominated by the grating). The coupling modulates the scene radiance slightly (Equation (1)), but also leaves a residual error due to the mirror emission that is different when looking in the space view than it is in the Earth view and OBC blackbody view (Equation (3)). The correction requires good knowledge of the product of the polarization factor for the scan mirror (p_r) and the spectrometer (p_t) and the phase of the spectrometer relative to the scan mirror while pointed at nadir (δ) [36].

For V5, we had individual measurements made pre-flight of the polarization of the scan mirror and completed spectrometer as well as a model that computed the polarization from measurements at the component level. The two models agreed well, except in the longest wavelengths. The approach taken for V5 was to average the measured and component results and apply a 5-point running median

filter for all channels. No attempt was made to separate polarization into A or B sides, and the phase was assigned to be zero for all channels, since, at the time, it was not possible to determine a value with sufficient confidence from the tests.

More recently, we were able to derive the polarization amplitude and phase, with good precision, directly from measurements in orbit while viewing space [29]. The set we derived are candidate coefficients for V7. The candidate V7 polarization amplitude and phase are determined by computing the signal difference of the space views acquired in orbit at 75°, 82°, and 101° relative to the space view at 91°, and fitting the difference to the radiometric calibration equations, ignoring second order terms, with $L_{ev} = 0$. Since the AIRS has space view data for every scan for the entire mission, we were able to compute the polarization and phase terms as a function of time from 2002 to 2017. Any change observed in the polarization is most likely due to degradation of the scan mirror, since the other elements are well isolated. We averaged the space view data into monthly averages, 171 months, to reduce noise. Data were grouped by PV detector side being used (A side, B side, or combined AB) for each channel prior to solving for the coefficients for each month. Coefficients were calculated for all valid channel and time periods. A linear fit to the coefficients, e.g., $p_r p_t$, in time gives an offset, $p_r p_t$_0, and a drift rate, $p_r p_t$_m, that can be used to compute the coefficient at any time in the life of the instrument. Offset and drift rates for A and B sides of channels not yet exercised on orbit are determined by a second order fit to all the channels in its module that have a valid coefficient on that side.

For the uncertainty in the polarization coefficients for V5, we include the difference between the V5 coefficients at launch and the V7 coefficients for October 2019. Use of the October 2019 polarization coefficients for V7 accounts for any observed drift that would have occurred due to mirror degradation. Figure 5a,b show the polarization amplitude and phase for Version 7 compared to Version 5 for module averages. The error bars in the figure represent the RMS deviation from a linear fit to the coefficients over the 171 months for V7. Since V5 used zero phase, the uncertainty in the phase term is the RSS of the V7 phase and the uncertainty in the V7 phase and the RMS deviation from the linear fit vs. time.

An additional contributor to the uncertainty in the polarization coefficients comes from independent in-orbit tests viewing the Right/Left (R/L) asymmetry [40]. In this analysis, the AIRS calibration subset product, AIRXBCAL, for V5 was used for 2016. This subset includes data from 50N to 50S for scenes with brightness temperature in channel 1231 cm^{-1} of less than 210 K mostly produced by deep convective clouds (DCCs). The average of signals from the right 1/3 of each scan was compared to the left 1/3 and a radiance difference calculated and converted to temperature. From the calibration equations (Equation (3)), a R/L asymmetry should result as a consequence of non-zero polarization and phase; if uncorrected it will show up as an asymmetry in the data. Figure 6 shows the R/L asymmetry observed for cold scenes), for the V5 product, and that predicted for V7 for the same data from the difference of V5 and V7. Since the phase of the polarization in V5 was zero, we should see no asymmetry, and the plotted asymmetry represents an error term. The predicted V7 polarization terms correct the asymmetry in most cases. Differences are seen in the LWIR channels with wavenumbers less than 800 cm^{-1}. Residual asymmetry is seen in the CrIS instrument at these wavelengths of the same sign (left is warmer than right) that may indicate the difference seen in Figure 6 is due to a geophysical difference. The time difference between the two views is approximately 50 minutes in mean local time. The difference seen in module M5 at 9.1 μm (1100 cm^{-1}) is at the peak of the scan mirror polarization and may indicate an underestimate in the polarization amplitude or incorrect phase in both V5 and V7. We see considerable drift in the predicted V7 asymmetry in this module as well. The average change to the $p_r p_t$ needed to zero out the L/R asymmetry at this wavelength is about 18%. We cannot determine whether the difference is due to the instrument or the measurement, so attribute half the error to each. We expect all channels to have a similar error. We therefore add a 10% 1-sigma (rounding up $\frac{1}{2}$ of the error) to all channels as the additional contributor to polarization uncertainty. The L/R asymmetry involves both polarization amplitude and phase;

however, we apply all the additional error to the amplitude, $p_r p_t$, as it is not possible to separate the error into the two contributors.

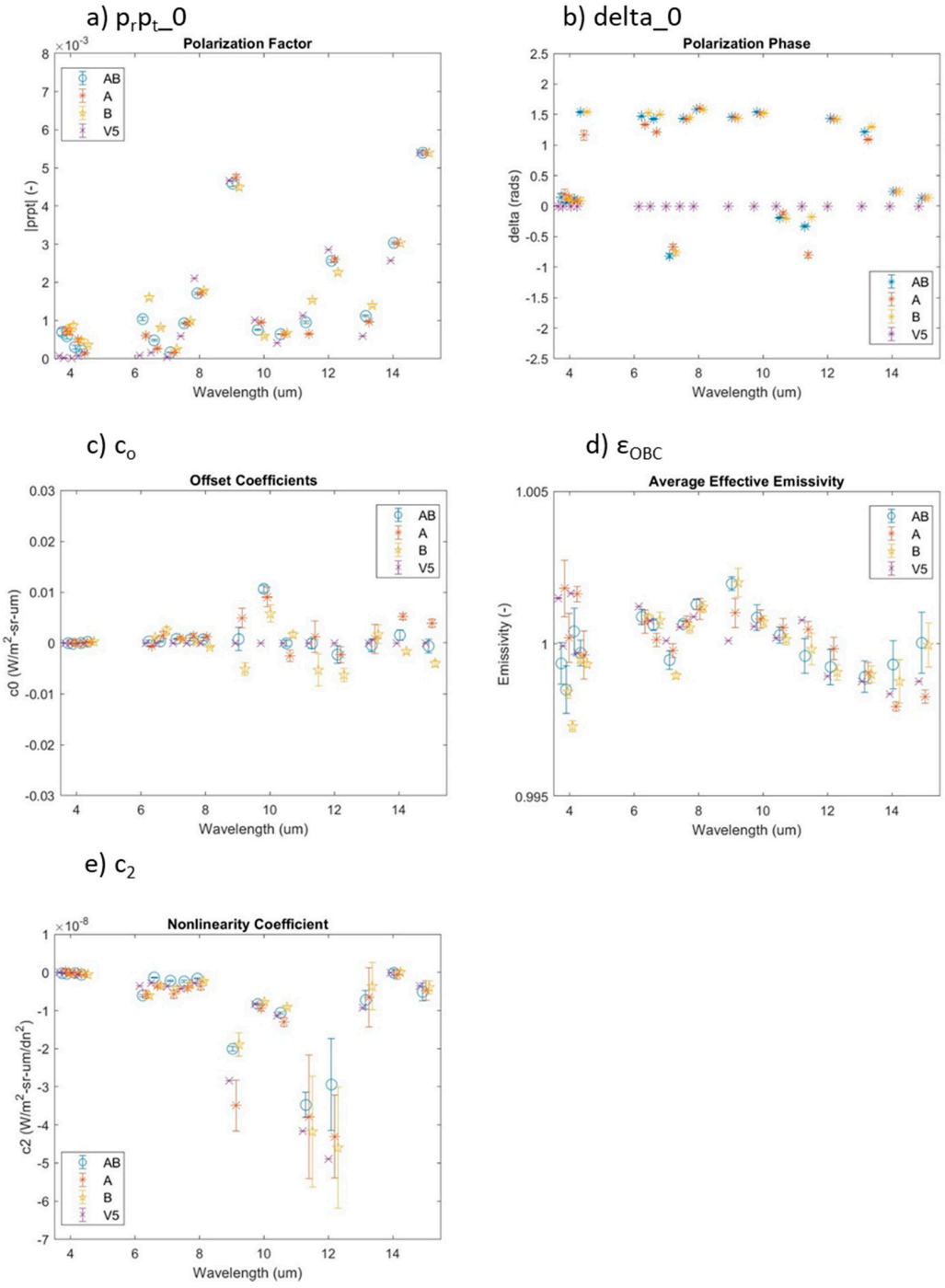

Figure 5. Module average coefficient values for V7 (labeled A, B, and AB for the PV detector sides in use during the test), and V5 (one side per channel). (**a**) Polarization factor of scan mirror and spectrometer interpolated to start of mission. (**b**) Phase of the spectrometer polarization interpolated to start of mission. (**c**) Offset coefficient. (**d**) Effective emissivity. (**e**) Nonlinearity coefficient. Error bars represent the standard deviation among the tests used to derive the coefficients; not the overall uncertainty in the coefficients. Error bars for V5 are not plotted since only one test per side was used to derive the coefficients.

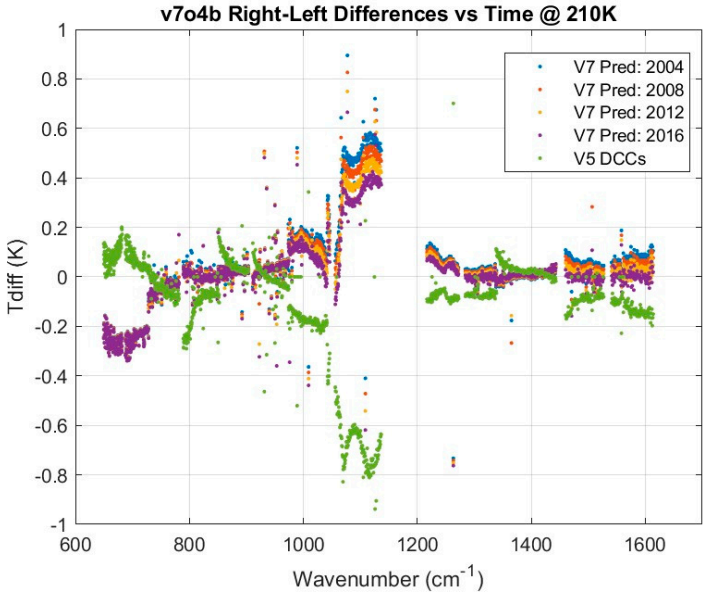

Figure 6. R/L asymmetry for V5 viewing cold scenes (<210 K), and that predicted for V7 by adjusting the V5 result. Differences lead to adding 10% 1-sigma to the $p_r p_t$ uncertainty.

2.6.3. Pre-Flight Radiometric Testing

Radiometric calibration and performance testing were performed under thermal vacuum conditions, at BAE SYSTEMS on October 29, and November 3, 1999. During testing, the AIRS viewed the LABB and SVS alternately while scanning. The LABB was stepped from 205 to 310 K over the course of 8 hours to calibrate the AIRS radiometric response. The SVS was held at a temperature of 85 K. The radiance of the LABB is computed as a Planck blackbody radiance distribution at the reported control temperature of the LABB. The radiances are fit to a polynomial in the difference in signals obtained between the LABB and SVS (Equation (1)). L_o is calculated using the polarization terms, prpt and δ, obtained from independent tests (see Section 2.6.2). The resulting coefficients obtained from the radiometric tests include the offset term, c_o, the emissivity (from c_1), and the nonlinearity coefficient, c_2. The coefficients from this test for V5 and V7 are shown in Figure 5c–e. The temperature of the OBC is determined from the telemetry with a correction of +0.3 K as discussed in Section 2.6.6, while the temperature of the scan mirror is taken directly from the telemetry of the scan mirror temperature sensor.

The AIRS is a multi-aperture system and was scanning while viewing the LABB. Image rotation causes the different apertures to scan the center of the LABB at slightly different positions. The LABB footprint with the full aperture illumination was found empirically, and an average signal was taken around a window of ±2 footprints on either side. For the tests made with the LABB at a scan angle of 40°, there is considerably more dispersion in the center footprints amongst the modules. We empirically determined that there is 1 sample/mm footprint offset of the samples in relation to the focal plane positions. Detector coordinates were used to offset the samples for each module relative to the center. The space view #1 was then subtracted on a scan by scan basis from the LABB and OBC data, and all scans averaged, to arrive at one signal number per LABB temperature per channel per test.

Table 5 gives the tests IDs used in the V5 calibration of AIRS. The data were acquired with the LABB at nadir. Some tests were not useful due to data problems. These were removed from the fits to the responses. For V5, coefficients are calculated for separate A and B for PV detector sides, then combined for a given state (1881_42) corresponding to the at-launch configuration. Coefficients for bad channels are computed as the median of the two coefficients on either side of the bad channel. Then a running 5-point median filter is applied to all coefficients for all channels within a module. This

'smoothing' reduces the impact of noise on the measurement uncertainty of the instrument, but could introduce errors when smoothing over channels with different AB PV detector sides.

Table 5. Tests used for determining the AIRS V5 radiometric calibration coefficients. LABB at nadir.

View\Temp(K)	205	220	230	240	250	265	280	295	310
A Side: Nadir	1687	1692	1693	1698 *	1704	1707 *	1718	1719	1727 *
B Side: Nadir	1688	1689	1696	1697	1705	1706	1715	1720	1726

* 1698: Saturated M4, 1707: zeros, 1727: low gain. These three tests were not used in the analysis.

While V7 is not officially released, and the coefficients are not finalized, we use the current candidate (V7o4, referred here simply as V7) for both the nominal values and uncertainty of the coefficients. There can still be small changes for the V7 L1B coefficients before their release in 2021, but we do not expect these to significantly impact our assessment of the V5 uncertainty. For V7, we chose to use more tests in the calculation of the coefficients and use the variance amongst the test to estimate the uncertainty in the coefficients. Table 6 lists the test used in addition to the tests in Table 5 to compute the V7 coefficients. For V7, coefficients are calculated for A, B, and AB separately and no smoothing is applied. The AB side configuration determined from in-flight test 359, performed in October 2019 is used. Errors introduced by changing AB sides over the mission and the smoothing process that are present in V5 should show up in the V5 uncertainty estimate when we take the difference from the V7 coefficients.

Table 6. Additional tests used for determining the AIRS V7 radiometric calibration coefficients.

View\Temp(K)	205	220	230	240	250	265	280	295	310
AB Side: nadir	1685	1690	1694	1699	1702	1708	1716	1721	1724
AB Side: nadir	1686	1691	1695	1700	1703	1709	1717	1722	1725
A Side: 40deg	1830	1841	1844	1849	1852	1857	1860	1865 *	1872
B Side: 40deg	1829	1842	1843	1850 *	1851 *	1858	1859	1866	1871
AB Side: 40deg	1832	1839	1845	1848	1853	1855	1861	1864	1869
AB Side: 40deg	1831	1840	1846	1847	1854	1856	1862	1863	1870

* 1865: Anomalous, 1850 Missing, 1851 Scan Dropout. These three tests were not used in the analysis.

2.6.4. Offset Coefficient, c_o

The offset coefficient, c_o, shown in Figure 5c, is the residual bias in the radiances for counts in the earth view equaling those in the space view. The offset will be non-zero, either for errors in the SVS and LABB calibration, conditions of the test, view factors of the instrument, or other factors. The offset varies from test to test as indicated by the length of the error bars, for the V7 points, that represents the standard deviation amongst the test. The instability in this coefficient from test to test observed preflight, combined with its small magnitude led us to set c_o to zero in Version 5, with the expectation that the full offset correction is contained in the polarization term L_o. The uncertainty, according to Equation (5), will include the full magnitude of offset (since V5 set this value to zero) RSS'd with the variability seen in the V7 offsets among the tests. Although we expect the existence of a non-zero c_o to be test related, the uncertainty in c_o predicted pre-flight is expected in-orbit and no time dependence is given to the uncertainty.

2.6.5. Nonlinearity Coefficient, c_2

The nonlinearity coefficient, c_2, shown in Figure 5e, is derived from pre-flight measurements, simultaneously with the gain coefficient c_1. The nonlinearity for Version 5 is computed as with the other coefficients, based on the PV detector A side and B side only tests and combined according to an AB side table (based on detector noise and responsivity), then smoothed. For V7, we compute the nonlinearity as the average of the A side nadir and 40° data for the A side detectors, and similarly for

the B side and combined AB independently. Before we take the difference with V5 when calculating the uncertainty, we apply the AB side to V7 from test 359 acquired in orbit in October 2019. The uncertainty for V7 is the standard deviation of the derived c_2 amongst all the tests for a given side.

As the gain changes in orbit due to optical factors, to first order, the nonlinearity must also change to obtain the same radiance [41]. We define the normalized nonlinearity coefficient as $c_2(1/c_1)^2$. The V7 nonlinearity is then multiplied by the square of the gain computed in-flight, c_1'. We use the most recent gains from test 359 in orbit for the V7 nonlinearity coefficient. The uncertainty in the drift due to the gain changes will be inherent in the V7-V5 differences. The impact of the gain change on the nonlinearity is less than 40 mK for most channels.

One nonlinearity test was performed in-orbit by turning off the OBC blackbody heater and measuring the response as the blackbody cooled. The test was performed shortly after launch, and while the data are a good check on the nonlinearity, they are insufficient to characterize the uncertainties or drift in the coefficients [41]. They do verify that separate A and B PV detector side nonlinearities should be carried in V7 corresponding to the on-orbit AB side configuration at any given time.

2.6.6. On Board Calibrator (OBC) Temperature Uncertainty

On-orbit, two-point radiometric calibrations are obtained every scan (2 2/3 s) by observing the OBC and deep space. This provides a continuous calibration of the radiometric gain of the instrument (radiance input to digital numbers output for each channel). The OBC carries the traceability established preflight to the on-orbit environment. A full aperture blackbody of a wedge design is also used on-board AIRS, which is very similar in construction to the LABB. The OBC blackbody, shown schematically in Figure 3, is servo controlled at 308 K. This temperature was chosen to be above the maximum temperature possible for the structure to which it mounts, but not too much above most observed warm scene temperatures. The cavity of the blackbody is constructed out of beryllium plates. Beryllium is lightweight and provides greater thermal conductivity than aluminum, providing very good temperature uniformity. As with the LABB, the aperture of the OBC is surrounded by a grooved, emissive plate held at very near the same temperature as the cavity, to again provide nearly the same radiance for any sensor out-of-field response as for its in-field response.

The cavity temperature is measured at three points and a fourth sensor measures the temperature of the aperture plate. Two sensors are on the directly viewed sloping surface and one of those is used by a servo-controlled heater to maintain a very constant cavity temperature. The two sloping surface sensors are read out at 10 mK resolution, the third cavity sensor is read out at 17 mK resolution and the aperture plate sensor is read out at 25 mK resolution. All four sensors are thermistors and were calibrated individually at NIST. The final calibration including the effects of sensor bias and the readout circuit was achieved by radiometric transfer from the LABB in ground calibration tests. Those tests showed that the indicated OBC temperature of 307.9 K needed to be offset by +0.3 K in a comparison of instrument response to the OBC with its response to the LABB at the same temperature. The offset accounts for two known factors in the electronics and the OBC temperature sensors. First, the Digital Number (DN) count at the control point temperature (308 K) is 830 while the calculations using the circuit diagram of the electronics say it should be 813. This accounts for 0.163 K. Secondly the NIST 78 μA thermistor current calibration was used instead of one using the actual bias current. Bias current causes heating (calculated using the power rule I^2R) and accounts for approximately 0.154 K. Based on this analysis and the observation, we use a nominal OBC temperature offset of +0.3 K. The OBC temperature offset is not considered a radiometric uncertainty. The uncertainty in the AIRS due to the OBC blackbody is from lack of perfect knowledge of the emitted radiance. Using a fixed temperature, globally, moves most of the uncertainty in the radiance into uncertainty of the 'effective' emissivity (see next section).

There is one additional small uncertainty in the temperature that remains in orbit; the variability in the temperature reading seen in orbit. We see orbital variation of 1.6, 4.0, 12.4, and 14.9 mK (1-sigma) for the 4 temperature sensors in the AIRS OBC blackbody. With the same theoretical weighting for

the temperature sensors of 0.45, 0.45, 0.09, 0.01 as used to compute the overall temperature, we get a variability of approximately 3.8 mK, 1-sigma. This value is carried in the V5 radiometric uncertainty estimate for the OBC temperature uncertainty and will also be present in V7.

2.6.7. On Board Calibrator (OBC) Effective Emissivity Uncertainty

The theoretical emissivity of the OBC can be determined as done for the LABB and SVS. The cavity interior surfaces are painted with Aeroglaze Z302 gloss black paint. The wedge angle is 23°, and rays in the direction that the cavity is viewed by AIRS make 7 bounces before exiting the cavity. Specular reflectance measurements of samples of the painted interior surfaces of the OBC turned out to be the same as for the paint used in the LABB. Using the same formalism described above for the LABB but for 7 bounces, the trap design emissivity is 0.999997. For the OBC, Ω = 0.6 sr for a point inside the cavity directly observed by AIRS. The BRDF measured for the painted interior walls (measured on witness samples) is 1×10^{-4} sr^{-1} at 3.39 μm and 2×10^{-4} sr^{-1} at 10.6 μm. From this the theoretical emissivity (at 10.6 μm) is calculated to be 0.99988. The radiometric uncertainty of the emitted radiance for the AIRS OBC is not determined by the theoretical emissivity uncertainty, but how well we can measure its emissivity relative to our standard, the LABB.

Multiple measurements while viewing the LABB allows us to establish an uncertainty in the emitted radiance based on measurements. We use the linear coefficient c_1 obtained in the stepped LABB tests, described above, to compute the OBC blackbody 'effective' emissivity. We call it an 'effective' emissivity as it is a measured quantity and shown in Figure 5d, along with the standard deviation in the measurement (error bars). By using a single fixed temperature for the OBC blackbody (see Section 2.6.6), the emissivity uncertainty includes biases and temperature gradients that occur within the OBC blackbody, as well as test related viewing geometry artifacts. For V5, the emissivity was calculated by measuring the linear coefficient, c_1, and solving for the emissivity per Equation (4). As done for the other coefficients in V5, the coefficients are calculated for the PV detector A side and B side and combined for the at-launch AB side configuration and smoothing as described above. For V7, emissivity is calculated for A side, B side and the combined AB sides separately and ultimately combined using the current AB side configuration. As for the other coefficients, the radiometric uncertainty is calculated as the difference between V5 and V7 RSS'd with the uncertainty in V7 and the drift.

2.6.8. OBC Emissivity Drift Uncertainty

The wedge cavity design of the OBC relies on mirror smooth black surfaces, configured as a light trap. What limits the cavity emissivity is the imperfect smoothness of the surface and scattering from particulates. Both effects can be quantified by the BRDF as done for the LABB. If the surface properties of the OBC change with time due to contamination or degradation, then the emissivity would most likely degrade. We have seen drifts in the apparent scene brightness temperature on the order of 10 mK/year at 2508 cm^{-1} for clear ocean scenes [42]. Using the radiometric calibration equations, we determined that the 10 mK/year drift could be accounted for by an emissivity change over the life of the mission of 0.008 at 2508 cm^{-1}. We can scale this drift to other wavelengths assuming a scattering wavelength dependence for smooth surfaces of λ^4 using the Angle-resolved scatter term [43].

$$\varepsilon_{obc}(\lambda_2, t_2) = \varepsilon_{obc}(\lambda_2, t_1) + [\varepsilon_{obc}(\lambda_1, t_2) - \varepsilon_{obc}(\lambda_1, t_1)]\frac{\lambda_1^4}{\lambda_2^4} \quad (9)$$

This uncertainty is included in the uncertainty estimate of the blackbody emissivity for Version 5.

Additional time dependent biases between channels, particularly in module M8 between PV detector A and B sides, may be related to using a single set of coefficients for A and B sides in Version 5, or polarization, offset, or emissivity drift [44]. At this time, we have not included the AB differences in M8 explicitly in the uncertainty budget since we expect the biases to be corrected by using separate

sides in the polarization and emissivity terms in this analysis for V7, and have already accounted for drifts in these terms.

2.6.9. Instrumental Noise and Drift

Random noise in the observed radiances is not included in the radiometric measurement uncertainty estimate as it averages to zero over large statistical samples. Random noise, or radiometric sensitivity, is expressed as the noise equivalent differential temperature (NEdT) for a scene temperature of 250 K. The NEdT for AIRS is measured by interpolating the noise while viewing cold space and the OBC at 308 K. Low frequency noise (or drift), and correlated noise can introduce biases, and both are included in the uncertainty estimate. The random noise (StdDev) and correlated noise (OffDiag) are shown in Figure 7.

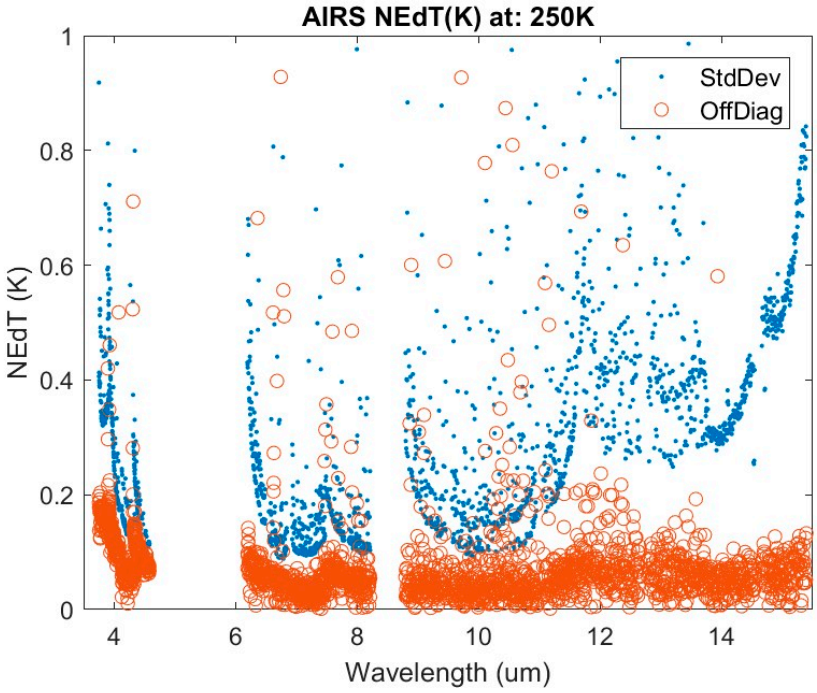

Figure 7. Noise equivalent differential temperature (NEdT) for AIRS at 250 K for uncorrelated (blue points) and correlated (red circles) noise. Correlated noise is considered a radiometric uncertainty.

Noise characterization for AIRS was performed by acquiring instrument digital output while viewing a known calibration target temperature. In this analysis, we use data acquired pre-flight with the AIRS mirror stationary to provide the most samples per scan and view the SVS. The signals for each of the 90 Earth sector footprints is subtracted from the median of the 4 space view samples as done in the flight algorithm. The signals are converted to radiances using the gains calculated from the OBC during a prior test while scanning. The noise equivalent radiance (NEN) is calculated for each channel as the standard deviation of the radiance timeseries. The derivative of the Planck blackbody radiance with respect to temperature at the scene temperate of 250 K is used to convert the NEN into a NEdT.

The noise covariance matrix is calculated from the SVS radiance timeseries for all channels into an $N_{ch} \times N_{ch}$ matrix. The correlated noise is calculated as the square root of the average magnitude of the off-diagonal terms of the noise covariance matrix. Other than channels failing or becoming noisy due to radiation, the AIRS noise levels and properties have been stable throughout the mission. We include all the correlated noise as a radiometric error since is it not guaranteed that a user will be able to account for the correlated errors in the radiometry.

Since the AIRS instrument calibrates once per scan line, any drift of the offset can introduce a radiometric error. A measure of this drift was made during the space view noise special test, described above, performed pre-launch and in orbit. The drift rate is calculated as the space view counts at the end of the period (over 600 scans) minus the counts at the start divided by the number of scans in the test period. Typically drift counts are in the range of 0.1–0.6 dn / scan. The correlated noise and drift are converted to a radiometric temperature error using the instrument nominal gain and included in the uncertainty estimates.

3. Results

The radiometric measurement uncertainty relative to SI-traceable standards for the AIRS L1B product is determined by taking the RSS of the uncertainty of all significant parameters in the radiometric calibration equation and that of the LABB and SVS. For the AIRS uncertainties, we calculate the radiometric contribution of each parameter by perturbing its value by the ±1-sigma uncertainty in a computer model of the radiometric calibration equation and dividing the result by two. The process is performed at a number of different scene temperatures for each channel of AIRS. Although uncertainties are carried individually for all 2378 channels, A, B and AB PV detector sides, module average uncertainties are shown that summarize the results.

Figure 8 shows the total module average accuracies (1-sigma relative to SI-traceable sensors in the LABB) as a function of temperature for V5. This figure highlights the high uncertainty in the M5 and M9 modules at low scene temperatures due to the higher polarization uncertainty in this module for in V5. It also highlights the higher errors associated with the emissivity degradation in the shorter wavelength modules. For most modules, we can expect around 250 mK 1-sigma uncertainty or better for scene temperatures greater than 260 K for Version 5. We expect better accuracies from the future V7 release as we account for the observed changes in the instrument behavior and improved statistics on the pre-flight test data.

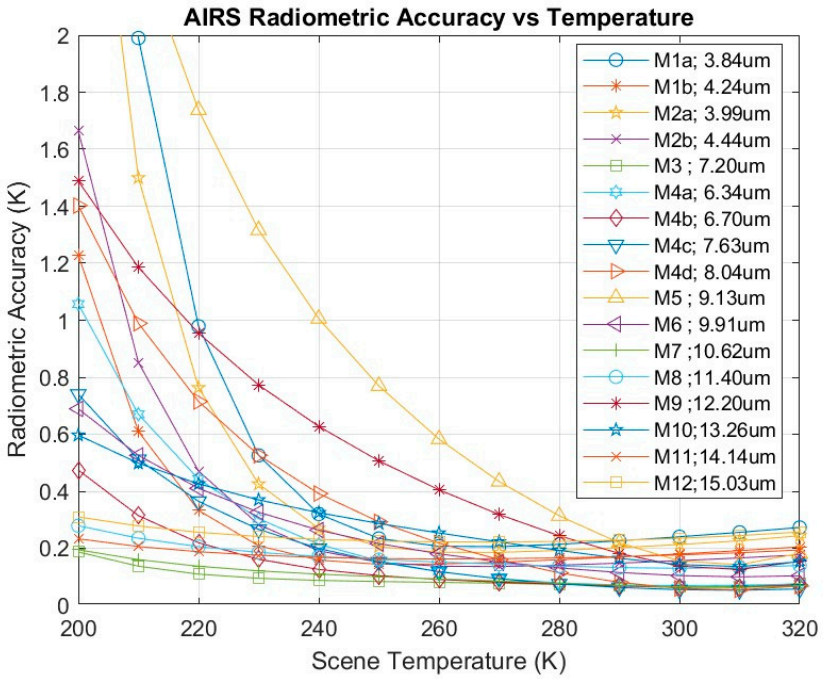

Figure 8. Radiometric uncertainty vs. temperature for V5.

Table 7 lists the resulting radiometric uncertainty for each contributor expressed as a temperature uncertainty for a scene temperature of 260 K. The uncertainties for the individual contributors for each

channel (see Table 2 for the list of contributors) are input into the radiometric calibration equation along with their nominal values (see Figure 5 for the module averages), and medians calculated over all channels in a module to arrive at the uncertainties listed in Table 7. The results are expressed graphically in Figure 9. The total uncertainties represent the 1-sigma measurement uncertainty of the AIRS V5 radiances relative to the SI-traceable sensors in the LABB.

Table 7. Radiometric measurement uncertainty by contributor for the median of all channels in a module. Uncertainties are expressed in terms of a temperature uncertainty for a scene temperature of 260 K. All uncertainties are 1-sigma. Contributors include (according to column order), LABB temperature uncertainty, ΔT_{LABB}, LABB emissivity uncertainty, $\Delta\varepsilon_{LABB}$, SVS temperature uncertainty, ΔT_{SVS}, SVS emissivity uncertainty, $\Delta\varepsilon_{SVS}$, scan mirror temperature uncertainty, ΔT_{SM}, scan angle uncertainty, $\Delta\theta$, polarization product uncertainty, $\Delta p_r p_t$, polarization phase uncertainty, $\Delta\delta$, offset coefficient uncertainty, Δa_o, nonlinearity coefficient uncertainty, Δa_2, OBC blackbody emissivity uncertainty, $\Delta\varepsilon_{OBC}$, OBC blackbody temperature uncertainty, ΔT_{OBC}, correlated noise, NEN_{corr}, and offset drift, Δdn.

Uncertainty	λ	ΔT_{LABB}	$\Delta\varepsilon_{LABB}$	ΔT_{SVS}	$\Delta\varepsilon_{SVS}$	ΔT_{SM}	$\Delta\theta$	$\Delta p_r p_t$	$\Delta\delta$	Δa_o	Δa_2	$\Delta\varepsilon_{OBC}$	ΔT_{OBC}	NEN_{corr}	Δdn_{drift}	RSS
Module	(μm)	(mK)	(mK)	(mK)	(mK)	(mK)	(mK)	(mK)	(mK)	(mK)	(mK)	(mK)	(mK)	(mK)	(mK)	(mK)
M1a	3.84	30.4	1.1	0.0	0.0	0.5	0.0	12.5	1.0	16.3	21.3	178.4	0.0	96.5	0.0	207.2
M1b	4.24	30.4	1.2	0.0	0.0	0.3	0.0	8.3	0.4	7.7	24.4	133.0	0.0	39.3	0.0	144.6
M2a	3.99	30.3	1.1	0.0	0.0	0.5	0.0	14.4	0.2	32.8	42.7	157.4	0.0	76.0	0.0	186.0
M2b	4.44	30.4	1.3	0.0	0.0	−0.2	0.0	7.3	10.0	19.0	15.3	114.5	0.0	62.7	0.0	136.9
M3	7.20	30.2	2.0	0.0	0.0	0.0	0.0	2.4	6.5	12.0	55.4	40.3	0.0	24.3	−8.1	80.3
M4a	6.34	30.3	1.8	0.0	0.0	−0.9	0.0	41.4	76.6	19.6	15.2	42.5	0.0	53.4	−7.9	117.6
M4b	6.70	30.3	1.9	0.0	0.0	−0.3	0.0	21.6	31.1	11.5	50.5	36.7	0.0	42.0	−4.1	90.3
M4c	7.63	30.2	2.2	0.0	0.0	−0.7	0.0	55.3	71.5	17.1	30.3	24.5	0.0	54.5	−7.0	117.9
M4d	8.04	30.3	2.3	0.0	0.0	−1.3	0.0	152.1	138.7	20.1	38.5	27.8	0.0	39.5	−5.4	218.1
M5	9.13	30.4	2.6	0.0	0.0	−3.3	−0.2	388.1	396.2	101.1	109.2	88.6	0.0	37.3	1.7	583.0
M6	9.91	30.2	2.8	0.1	0.0	−0.6	0.0	82.8	71.0	119.2	50.3	44.7	0.0	31.8	1.2	180.5
M7	10.62	30.2	3.0	0.2	0.0	0.4	0.0	16.8	4.5	43.3	57.2	29.9	0.0	35.9	2.1	92.4
M8	11.40	30.1	3.2	0.4	0.0	0.5	0.1	9.4	12.5	85.3	75.6	78.3	0.0	51.7	6.5	151.6
M9	12.20	30.2	3.4	0.8	0.0	−1.5	−0.1	258.8	250.4	108.8	117.6	63.1	0.0	60.8	6.5	405.0
M10	13.26	30.1	3.7	1.7	0.0	−0.5	−0.1	72.6	107.6	132.4	148.1	59.9	0.0	58.6	7.7	253.6
M11	14.14	30.0	3.9	2.8	0.0	1.6	−0.2	29.9	18.5	75.8	40.8	122.1	0.0	44.0	0.0	162.5
M12	15.03	29.9	4.1	4.5	0.0	2.9	−0.2	43.9	11.6	110.7	68.3	160.2	0.0	62.9	0.0	222.5

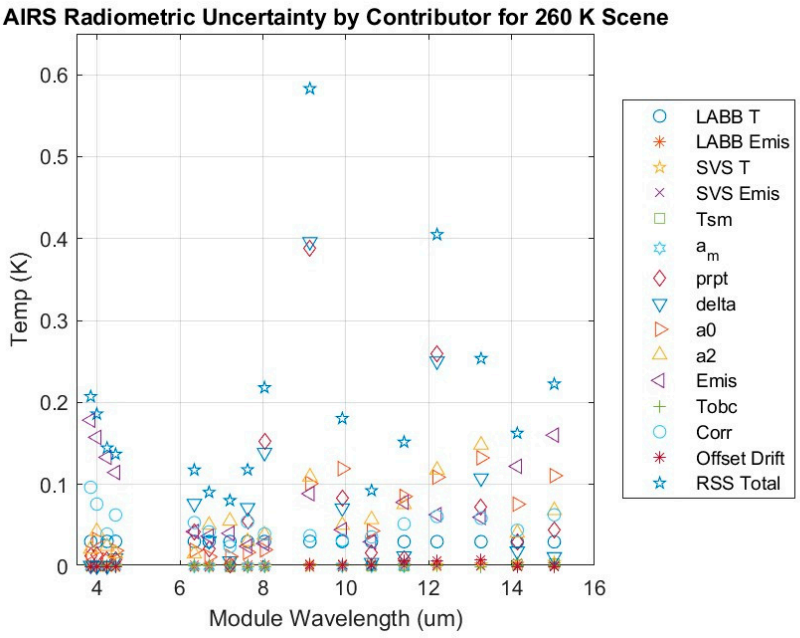

Figure 9. Module median radiometric uncertainties for V5 for each of the contributors expressed at 260 K scene temperature. Uncertainties represent the 1-sigma deviation from the SI-traceable sensors in the LABB.

4. Discussion

The Atmospheric Infrared Sounder (AIRS) on the Aqua spacecraft measures the upwelling radiance in the infrared in over 2378 channels with spectral resolutions ranging from 3 nm (2.1 cm^{-1}) at 3.7 μm to 10 nm (0.41 cm^{-1}) at 15.4 μm. The instrument includes an OBC Blackbody and views of space every scan. The instrument radiometric calibration is performed pre-launch using calibration targets, the LABB and the SVS and transferred to the OBC blackbody during pre-launch testing. Although the SVS temperature sensors are not SI-traceable, their contribution to the measurement uncertainty and SI-traceability is negligible since the SVS operates at 85 K and SI-traceability is established through the LABB. The radiometric measurement uncertainty of AIRS is computed as the RSS of the uncertainty in the ground calibration targets and the measurement uncertainty in the AIRS instrument. We evaluate the measurement uncertainty of AIRS as the RSS of the uncertainty in the radiometric calibration coefficients (obtained while viewing the LABB) and estimated changes in the OBC emissivity, mirror polarization, correlated noise, and drift during a scan line. The uncertainties account for drift over time of the coefficients, and changes in AB side of the detector pairs. They include the systematic errors (difference between our current understanding of the mean for V7 and what we have for V5), and the uncertainty in our V7 coefficients.

In modules M5 and M9, the uncertainty is limited by mirror polarization uncertainty, particularly at cold scene temperatures. The error appears as an offset in the calibration and is more noticeable in cold scenes. A much better estimate of the polarization amplitude and phase is in hand that will greatly reduce this error and is planned for inclusion in a future version of L1B (V7). Despite the uncertainty in these modules, the AIRS V5 L1B radiances show excellent radiometric measurement uncertainty, particularly in M3, M4b and M7 with under 100 mK uncertainty at 260 K for most channels in the modules (not including spatial or spectral errors).

Although not presented here, the AIRS also has excellent radiometric stability, enabling the pre-flight calibration to be applied throughout the mission without changes as done in V5. Small changes in what appears to be the properties of the scan mirror and blackbody can be seen in the data. In-flight characterization using the space views and OBC blackbody and Earth scenes, such as DCCs and SST, has led to a better understanding of the AIRS performance and will enable a considerable reduction in the measurement uncertainty in a future version of the L1B (V7).

Future instruments would benefit by having OBC blackbodies that are accurate at multiple temperatures, and deep-space views to characterize mirror polarization; however, low radiometric measurement uncertainty is more than having an accurate on-orbit SI-traceable blackbody. Designers of future instruments requiring a high level of accuracy must consider uncertainties for all the terms that contribute to the radiometric calibration equation in-orbit based on their individual instrument design. As done here where possible, uncertainties in the verification of coefficients should be included in the overall radiometric measurement uncertainty, not just theoretical estimates.

5. Conclusions

The radiometric measurement uncertainty in the AIRS L1B V5 ranges amongst the channels from <100 to 600 mK (1-sigma) at 260 K scene temperature, with most channels below 250 mK. The estimated uncertainty of AIRS can be said to be very good considering the instrument was intended to be used for weather forecasting, where biases are tuned out. Many channels with accuracies estimated to be less than 100 mK are available in AIRS. Improvements to the calibration coefficients for V7, expected to be released in 2021, will reduce uncertainties in the worst affected channels with new estimates of the polarization, and reduced errors associated with the nonlinearity, emissivity and A vs. B detector dependence. Spectral and spatial errors are not included in our analysis since they are scene dependent. The spectral and spatial response functions are well known and should be used for small numbers of samples and high contrast scenes.

The radiometric measurement uncertainty of AIRS L1B V5 may be better than estimated here, but we are limited by our ability to verify it. We employ minimal use of theoretical estimates of the

uncertainty, primarily only to the LABB and SVS. But even here, we use component measurements of the surface properties. An independent test of the LABB to SI traceable standards would have been a good idea but was not made due to cost limitations. However, we see that the dominant sources of error in AIRS are related to the instrument design. Primarily, the use of a silver scan mirror to achieve high reflectance in the visible and near infrared (Vis/NIR) channels introduced polarization in the infrared, whereas a gold mirror would have made this error smaller (at the cost of lower reflectance in the Vis/NIR). Finally, while the OBC blackbody was an exceptionally stable standard, an in-orbit SI-traceable blackbody that operates at two widely separated temperatures with phase transition thermistors, and in-orbit reflectance measurements would have reduced many of the errors associated with transferring the calibration from the LABB to the OBC blackbody [45].

The good stability of the instrument enables less frequent tuning at data assimilation centers (for weather forecasting and reanalysis) and for the physical retrievals produced by the AIRS project. However, high accuracy is needed by those who use AIRS as a calibration reference through GSICS, for developers of reanalysis and RTMs, or scientists interested in climate benchmarking. The quantification of radiometric uncertainties and the resulting radiometric measurement uncertainty of the AIRS V5 radiance product presented here allows those who use V5 to propagate these uncertainties into their model or retrieval algorithms.

Author Contributions: Conceptualization: T.S.P. and K.O.O., methodology, T.S.P., software, T.S.P., C.C. and S.E.B., validation, H.H.A., E.M.M. and R.C.W., formal analysis, T.S.P., C.C. and K.O.O., investigation, T.S.P., resources, T.S.P., data curation, E.M.M. and S.E.B., writing-original draft preparation, T.S.P. and K.O.O., writing-review and editing, T.S.P. and K.O.O. All authors have read and agreed to the published version of the manuscript.

Funding: This research was funded by the National Aeronautics and Space Administration, Science Missions Directorate, Earth Science Division, Flight Projects, under the Aqua AIRS project.

Acknowledgments: The research was carried out at the Jet Propulsion Laboratory, California Institute of Technology, under a contract with the National Aeronautics and Space Administration. The authors would like to thank Margaret H. Weiler retired from BAE Systems, and Larrabee Strow of UMBC for their advice in the radiometric calibration and measurement uncertainty estimates.

Conflicts of Interest: The authors declare no conflict of interest. The funders had no role in the design of the study; in the collection, analyses, or interpretation of data; in the writing of the manuscript, or in the decision to publish the results.

References

1. Chahine, M.T.; Pagano, T.S.; Aumann, H.H.; Atlas, R.; Barnet, C.; Blaisdell, J.; Chen, L.; Divakarla, M.; Fetzer, E.J.; Goldberg, M.; et al. AIRS: Improving Weather Forecasting and Providing New Data on Greenhouse Gases. *Bull. Am. Meteorol. Soc.* **2006**, *87*, 911–926. [CrossRef]
2. Han, Y.; Revercomb, H.; Cromp, M.; Gu, D.; Johnson, D.; Mooney, D.; Scott, D.; Strow, L.; Bingham, G.; Borg, L.; et al. Suomi NPP CrIS measurements, sensor data record algorithm, calibration and validation activities, and record data quality. *J. Geophys. Res. Atmos.* **2013**, *118*, 12734–12748. [CrossRef]
3. Chalon, G.; Astruc, P.; Hébert, P.; Blumstein, D.; Buil, C.; Carlier, T.; Clauss, A.; Siméoni, D.; Tournier, B. IASI Instrument: Technical Description and Measured Performances. In *ESA ICSO, Proceedings of the 5th International Conference on Space Optics, Toulouse, France, 30 March–2 April 2004*; Costeraste, J., Armandillo, E., Eds.; SPIE: Bellingham, WA, USA, 2004; Volume 10568, pp. 1056806-1–1056806-9.
4. Carminati, F.; Xiao, X.; Lu, Q.; Atkinson, N.; Hocking, J. Assessment of the Hyperspectral Infrared Atmospheric Sounder (HIRAS). *Remote Sens.* **2019**, *11*, 2950. [CrossRef]
5. Yang, J.; Zhang, Z.; Wei, C.; Lu, F.; Guo, Q. Introducing the New Generation of Chinese Geostationary Weather Satellites, Fengyun-4. *Bull. Amer. Meteorol. Soc.* **2017**, *98*, 1637–1658. [CrossRef]
6. Timofeyev, Y.M.; Uspensky, A.B.; Zavelevich, F.S.; Polyakov, A.V.; Virolainen, Y.A.; Rublev, A.N.; Kukharsky, A.V.; Kiseleva, J.V.; Kozlov, D.A.; Kozlov, I.A.; et al. Hyperspectral infrared atmospheric sounder IKFS-2 on "Meteor-M" No. 2–Four years in orbit. *J. Quant. Spectrosc. Radiat. Transf.* **2019**, *238*. [CrossRef]

7. Marshall, J.L.; Jung, J.; Derber, J.; Chahine, M.; Treadon, R.; Lord, S.J.; Goldberg, M.; Wolf, W.; Liu, H.C.; Joiner, J.; et al. Improving Global Analysis and Forecasting with AIRS. *Bull. Am. Meteorol. Soc.* **2006**, *87*, 891–894. [CrossRef]
8. Pierce, D.W.; Barnett, T.P.; Fetzer, E.J.; Gleckler, P.J. Three-dimensional tropospheric water vapor in coupled climate models compared with observations from the AIRS satellite system. *Geophys. Res. Lett.* **2006**, *33*, L21701:1–L21701:5. [CrossRef]
9. Realmuto, V.J.; Berk, A. Plume Tracker: Interactive mapping of volcanic sulfur dioxide emissions with high-performance radiative transfer modeling. *J. Volcanol. Geotherm. Res.* **2016**, *327*, 55–69. [CrossRef]
10. Behrangi, A.; Fetzer, E.J.; Granger, S.L. Early detection of drought onset using near surface temperature and humidity observed from space. *Int. J. Remote Sens.* **2016**, *37*, 3911–3923. [CrossRef]
11. Adame, J.A.; Lope, L.; Hidalgo, P.J.; Sorribas, M.; Gutiérrez-Álvarez, I.; del Águila, A.; Saiz-Lopez, A.; Yela, M. Study of the exceptional meteorological conditions, trace gases and particulate matter measured during the 2017 forest fire in Doñana Natural Park, Spain. *Sci. Total Environ.* **2018**, *645*, 710–720. [CrossRef]
12. Susskind, J.; Schmidt, G.A.; Lee, J.N.; Iredell, L. Recent global warming as confirmed by AIRS. *Environ. Res. Lett.* **2019**, *14*, 044030:1–044030:10. [CrossRef]
13. Aumann, H.H.; Broberg, S.; Manning, E.; Pagano, T. 2019: Radiometric Stability Validation of 17 Years of AIRS Data Using Sea Surface Temperatures. *Geophys. Res. Lett.* **2019**, *46*, 12504–12510. [CrossRef]
14. Strow, L.L.; DeSouza-Machado, S. Establishment of AIRS Climate-Level Radiometric Stability using Radiance Anomaly Retrievals of Minor Gases and SST. *Atmos. Meas. Tech. Discuss.* **2020**, *2020*, 1–35. [CrossRef]
15. Dee, D.P.; Uppala, S.M.; Simmons, A.J.; Berrisford, P.; Poli, P.; Kobayashi, S.; Andrae, U.; Balmaseda, M.A.; Balsamo, G.; Bauer, P.; et al. The ERA-Interim reanalysis: Configuration and performance of the data assimilation system. *Q. J. R. Meteorol. Soc.* **2011**, *137*, 553–597. [CrossRef]
16. Rienecker, M.M.; Suarez, J.J.; Gelaro, R.; Todling, R.; Bacmeister, J.; Liu, E.; Bosilovich, M.G.; Schubert, S.D.; Takacs, L.; Kim, G.-K.; et al. MERRA: NASA's Modern-Era Retrospective Analysis for Research and Applications. *J. Clim.* **2011**, *24*, 3624–3648. [CrossRef]
17. Goldberg, M.; Ohring, G.; Butler, J.; Cao, C.; Datla, R.; Doelling, D.; Gartner, V.; Hewison, T.; Iacovazzi, B.; Kim, D.; et al. The global space-based inter-calibration system. *Bull. Am. Meteorol. Soc.* **2011**, *92*, 467–475. [CrossRef]
18. GSICS Traceability Statement for IASI and AIRS. EUMETSAT Document: EUM/MET/TEN/11/0157. 2014, pp. 1–11. Available online: https://www.eumetsat.int/website/wcm/idc/idcplg?IdcService=GET_FILE&dDocName=PDF_TRACE_STAT_IASI_AIRS&RevisionSelectionMethod=LatestReleased&Rendition=Web (accessed on 2 April 2020).
19. Meteorological Satellite Center (MSC) of JMA, GSICS Infrared Inter-calibration, Himawari-8,9/AHI IR Inter-Calibration with AIRS, IASI, and CrIS. Available online: https://www.data.jma.go.jp/mscweb/data/monitoring/gsics/ir/monit_geoleoir.html (accessed on 18 February 2020).
20. KMA's Activities of GSICS, 2nd Teleconference Meeting. 16 December 2008; pp. 1–14. Available online: https://www.star.nesdis.noaa.gov/smcd/GCC/documents/GRWG/200812/Pres_Kim_KMA_081216GRWG_WebMtg.pdf (accessed on 18 February 2020).
21. Tobin, D.; Revercomb, H.; Knuteson, R.; Taylor, J.; Best, F.; Borg, L.; DeSlover, D.; Martin, G.; Buijs, H.; Esplin, M.; et al. Suomi-NPP CrIS radiometric calibration uncertainty. *J. Geophys. Res.-Atmos.* **2013**, *118*, 10589–10600. [CrossRef]
22. Wu, X.; Yu, F. Correction for GOES Imager Spectral Response Function Using GSICS. Part I: Theory. *IEEE Trans. Geosci. Remote Sens.* **2013**, *51*, 1215–1223. [CrossRef]
23. Hilton, F.; Armante, R.; August, T.; Barnet, C.; Bouchard, A.; Camy-Peyret, C.; Capelle, V.; Clarisse, L.; Clerbaux, C.; Coheur, P.-F.; et al. Hyperspectral Earth Observation from IASI: Four years of accomplishments. *Bull. Am. Meteorol. Soc.* **2011**, *93*, 347–370. [CrossRef]
24. Kacker, R.; Yoon, H. Guidelines for Radiometric Calibration of Electro-Optical Instruments for Remote Sensing. In *NIST Handbook 157*; U.S. Department of Commerce: Gaithersburg, MD, USA, 2015. [CrossRef]
25. JCGM 200:2012, International Vocabulary of Metrology—Basic and General Concepts and Associated Terms (VIM Third Edition). 2012. Available online: http://www.bipm.org/utils/common/documents/jcgm/JCGM_200_2012.pdf (accessed on 2 April 2020).

26. JCGM 100:2008, Evaluation of Measurement Data—Guide to the Expression of Uncertainty in Measurement (GUM), BIPM, IEC, IFCC, ISO, IUPAC, IUPAP, OIML. 2008. Available online: https://www.bipm.org/utils/common/documents/jcgm/JCGM_100_2008_E.pdf (accessed on 2 April 2020).
27. Pagano, T.S.; Aumann, H.H.; Schindler, R.; Elliott, D.; Broberg, S.; Overoye, K.; Weiler, M. Absolute radiometric calibration accuracy of the Atmospheric Infrared Sounder (AIRS). In *Earth Observing Systems XIII, Proceedings of SPIE Optical Engineering + Applications, San Diego, CA, USA, 10–14 August 2008*; SPIE: Bellingham, WA, USA, 2008; Volume 7081, pp. 70811B-1–70811B-12.
28. Pagano, T.S.; Aumann, H.H.; Broberg, S.; Manning, E.; Overoye, K.; Weiler, M. Updates to the absolute radiometric accuracy of the AIRS on Aqua. In *Earth Observing Missions and Sensors: Development, Implementation, and Characterization V, Proceedings of SPIE Asia-Pacific Remote Sensing, Honolulu, HI, USA, 23 October 2018*; SPIE: Bellingham, WA, USA, 2018; Volume 10781, pp. 107810P-1–107810P-7. [CrossRef]
29. Pagano, T.S.; Manning, E.M.; Broberg, S.; Aumann, H.; Weiler, M.; Strow, L. Reducing uncertainty in the AIRS radiometric calibration. In *Earth Observing Systems XXIII, Proceedings of SPIE Optical Engineering + Applications, San Diego, CA, USA, 7 September 2018*; SPIE: Bellingham, WA, USA, 2018; Volume 10764, pp. 10764ON-1–10764ON-9.
30. Aumann, H.H.; Broberg, S.; Elliott, D.; Gaiser, S.; Gregorich, D. Three years of Atmospheric Infrared Sounder radiometric calibration validation using sea surface temperatures. *J. Geophys. Res.* **2006**, *111*, 1–8. [CrossRef]
31. Wang, L.; Han, Y.; Jin, X.; Chen, Y.; Tremblay, D.A. Radiometric consistency assessment of hyperspectral infrared sounders. *Atmos. Meas. Tech.* **2015**, *8*, 4831–4844. [CrossRef]
32. Pagano, T.S.; Aumann, H.H.; Manning, E.M.; Elliott, D.A.; Broberg, S.E. Improving AIRS radiance spectra in high contrast scenes using MODIS. In *Earth Observing Systems XX, Proceedings of SPIE Optical Engineering + Applications, San Diego, CA, USA, 8 September 2015*; SPIE: Bellingham, WA, USA, 2015; Volume 9607, pp. 9607-K-1–9607-K-10. [CrossRef]
33. Strow, L.L.; Hannon, S.E.; De-Souza Machado, S.; Motteler, H.E.; Tobin, D.C. Validation of the Atmospheric Infrared Sounder radiative transfer algorithm. *J. Geophys. Res.-Atmos.* **2006**, *111*, 1–24. [CrossRef]
34. Manning, E.M.; Strow, L.L.; Aumann, H. AIRS version 6.6 and version 7 level-1C products. In *Earth Observing Systems XXIV, Proceedings of SPIE Optical Engineering + Applications, San Diego, CA, USA, 9 September 2019*; SPIE: Bellingham, WA, USA, 2019; Volume 11127, pp. 1112718-1–1112718-7. [CrossRef]
35. Morse, P.G.; Bates, J.C.; Miller, C.R.; Chahine, M.T.; O'Callaghan, F.; Aumann, H.H.; Kamik, A.R. Development and test of the Atmospheric Infrared Sounder (AIRS) for the NASA Earth Observing System (EOS). In *Sensors, Systems, and Next-Generation Satellites III, Proceedings of Remote Sensing, Florence, Italy, 28 December 1999*; Society of Photo-optical Instrumentation Engineers: Bellingham, WA, USA; Volume 3870, pp. 281–292. [CrossRef]
36. Pagano, T.S.; Aumann, H.H.; Hagan, D.E.; Overoye, K.R. Prelaunch and In-Flight Radiometric Calibration of the Atmospheric Infrared Sounder (AIRS). *IEEE Trans. Geosci. Remote Sens.* **2003**, *41*, 265–273. [CrossRef]
37. Villemaire, A. Giroux, Jacques, Giroux, Jean, On-Ground IR Calibration Sources for AIRS. In Proceedings of the 6th Infrared Radiometric Sensor Calibration Symposium, Logan, UT, USA, 7–9 May 1996.
38. Villemaire, A. *AIRS Space View Black Body and Large Area Black Body, SVBB & LABB User's Manual*, 1st ed.; Bomem Inc.: Quebec City, QC, Canada, 1996; pp. 1–55, Document No. AI-BOM-022/96, CDRL No. A008.
39. Villemaire, A. *AIRS Large Area Blackbody Acceptance Report*, 1st ed.; Bomem Inc.: Quebec City, QC, Canada, 1996; Appendix B, Sp. 24, Document No. AI-BOM-039/96, CDRL No. A009.
40. Manning, E.M.; Aumann, H.H. Hyperspectral sounder performance for cold scenes. In *Earth Observing Systems XXII, Proceedings of SPIE Optical Engineering + Applications, San Diego, CA, USA, 5 September 2017*; SPIE: Bellingham, WA, USA, 2017; Volume 10402, pp. 1040225-1–1040225-10. [CrossRef]
41. Pagano, T.S.; Manning, E.M.; Broberg, S.E.; Aumann, H.H. Checking AIRS nonlinearity in flight. In *Earth Observing Systems XXIV, Proceedings of SPIE Engineering + Applications, San Diego, CA, USA, 9 September 2019*; SPIE: Bellingham, WA, USA, 2019; Volume 11127, pp. 1112717-1–1112717-7. [CrossRef]
42. Aumann, H.H.; Manning, E.M.; Broberg, S. Radiometric stability in 16 years of AIRS hyperspectral infrared data. In *Earth Observing Systems XXIII, Proceedings of SPIE Optical Engineering + Applications, San Diego, CA, USA, 7 September 2018*; SPIE: Bellingham, WA, USA, 2018; Volume 10764, pp. 107640O-1–107640O-7. [CrossRef]
43. Krywonos, A.; Harvey, J.E.; Choi, N. Linear systems formulation of scattering theory for rough surfaces with arbitrary incidence and scattering angles. *J. Opt. Soc. Am. A* **2011**, *28*, 1121–1138. [CrossRef] [PubMed]

44. Manning, E.M.; Aumann, H.H.; Kahn, B.H. Stratified radiometric means for the evaluation of AIRS and CrIS. In *Earth Observing Systems XXIII, Proceedings of SPIE Optical Engineering + Applications, San Diego, CA, USA, 7 September 2018*; SPIE: Bellingham, WA, USA, 2018; Volume 10764, pp. 107640P-1–107640P-14. [CrossRef]
45. Taylor, J.K.; Revercomb, H.E.; Best, F.A.; Knuteson, R.O.; Tobin, D.C.; Gero, J.P.; Adler, D.; Mulligan, M. An on-orbit infrared intercalibration reference standard for decadal climate trending of the Earth. In *Sensors, Systems, and Next-Generation Satellites XXIII, Proceedings of the SPIE, 10 October 2019*; SPIE: San Diego, CA, USA, 2019; Volume 111516. [CrossRef]